

# Temporal Bragg Gratings: Broadband Reconfigurable Parametric Amplifiers

Sajjad Taravati, *Senior Member, IEEE*

**Abstract**—This paper introduces temporal Bragg gratings as a new class of broadband, reconfigurable parametric amplifiers. We present a comprehensive investigation of power amplification in these structures, where a spatially periodic refractive index profile is modulated in time at frequencies near the Bragg condition. Through systematic numerical simulations, we explore the impact of modulation location (high-index vs. low-index layers), modulation frequency relative to the Bragg frequency, and modulation amplitude on the gain spectrum and field dynamics. We demonstrate that both high-index and low-index layer modulations can produce significant parametric amplification, with high-index modulation yielding higher gain for comparable modulation depths. The amplification is frequency-agile, with gain peaks tunable across a broad spectral range, and exhibits strong asymmetry between sub-Bragg and supra-Bragg regimes, the former requires substantially stronger modulation for comparable gain. In the extreme sub-Bragg limit, the system transitions from discrete sideband amplification to a broadband gain continuum at high frequencies, explained by multi-phase-matching of parametric processes. These results provide a unified framework for designing dynamically reconfigurable optical amplifiers, tunable frequency converters, and broadband light sources using temporally modulated photonic crystals, offering new pathways toward active, agile, and integrable photonic devices.

**Index Terms**—Temporal photonic crystals, parametric amplification, Bragg gratings, modulated photonic structures, tunable photonic devices, nonlinear optics

## I. INTRODUCTION

The control of light propagation through engineered materials has been revolutionized by the concepts of photonic crystals, gratings and metamaterials, which enable unprecedented manipulation of electromagnetic waves in both space and frequency domains [1]–[9]. By introducing periodic variations in the refractive index, spatial photonic crystals and Bragg gratings, researchers have demonstrated remarkable phenomena such as photonic bandgaps, slow light, and enhanced nonlinear interactions for sensing and biomedical applications [10]–[16]. More recently, the paradigm of temporal photonics has emerged, where material properties are modulated in time and space, unlocking fundamentally new degrees of freedom for controlling light [17]–[31].

Temporal modulation breaks time-reversal symmetry and enables nonreciprocal behavior [9], [23], [32]–[34], frequency conversion [7], [35]–[40], amplification without traditional gain media [18], [33], [41]–[45], and quantum frequency multiplexing and nonreciprocity [5], [30], [40], [46]. When

S. Taravati is with the Faculty of Engineering and Physical Sciences, University of Southampton, Southampton SO17 1BJ, UK (e-mail: s.taravati@soton.ac.uk).

combined with spatial periodicity, as in spatio-temporal photonic crystals or temporal Bragg gratings, rich interference phenomena arise that can lead to momentum bandgaps, parametric amplification, and frequency generation. A particularly intriguing regime occurs when the temporal modulation frequency  $\omega_m$  coincides with the Bragg frequency  $\omega_B$  of the underlying spatial grating, a condition known as coherent temporal modulation. In this configuration, the interplay between spatial and temporal periodicity can transform a passive photonic bandgap structure into an active amplifier, where incident waves experience exponential growth rather than reflection.

This study introduces and explores the concept of temporal Bragg gratings, spatially periodic structures modulated coherently in time, and demonstrate that they enable huge, dynamically reconfigurable power amplification. Through a comprehensive numerical and analytical study, we show how this emerging platform can be transformed from a passive filter into a powerful active device. We systematically investigate the role of key parameters—including modulation location (high-index vs. low-index layers), modulation frequency relative to the Bragg condition, and modulation amplitude—to map the resulting gain spectra and electromagnetic field distributions, revealing unprecedented control over amplification strength and spectral agility. Our results reveal that

- Frequency-agile amplification is achievable by detuning  $\omega_m$  from  $\omega_B$ , enabling tunable gain peaks at frequencies  $\omega_B \pm \omega_m$ .
- A pronounced asymmetry exists between the sub-Bragg ( $\omega_m < \omega_B$ ) and supra-Bragg ( $\omega_m > \omega_B$ ) regimes, with the former requiring significantly stronger modulation for comparable gain.
- In the extreme sub-Bragg limit ( $\omega_m \lesssim 0.1\omega_B$ ), the system transitions from discrete sideband amplification to broadband gain at high frequencies, explained by multi-phase-matching of non-degenerate four-wave mixing processes.
- Both high-index and low-index modulation can produce strong amplification.

Our findings provide a unified framework for understanding amplification in temporal photonic crystals and offer practical guidelines for designing reconfigurable optical amplifiers, frequency converters, and broadband light sources using temporal modulation. By mapping the parameter space of modulation frequency, amplitude, and location, this work establishes temporal Bragg gratings as versatile platforms for active photonic devices with dynamically controllable spectral response.

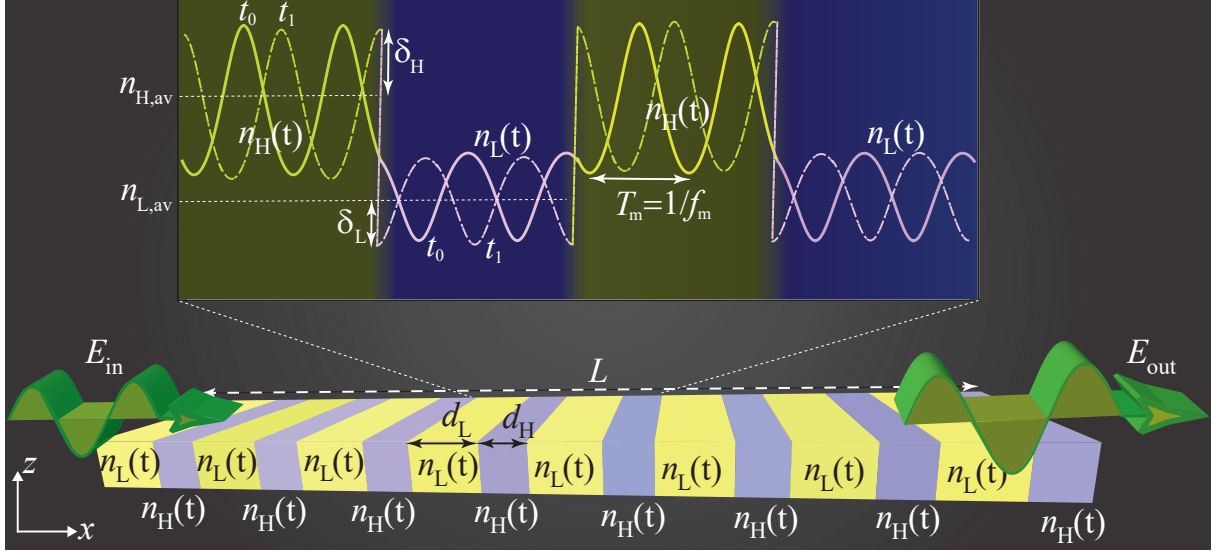


Fig. 1. Schematic of a temporal Bragg grating for through-port parametric amplification, composing alternating time-periodic high-index ( $n_H(t)$ ) and low-index ( $n_L(t)$ ) refractive indices.

## II. THEORETICAL IMPLICATIONS

### A. Temporal Bragg Grating Architecture

A Bragg grating is a periodic structure composed of alternating layers with high ( $n_H$ ) and low ( $n_L$ ) refractive indices, each having an optical thickness of  $\lambda_B/4$  at the design wavelength  $\lambda_B$ . This quarter-wave condition ensures constructive interference of reflections from each interface, creating a photonic stopband centered at the Bragg frequency  $\omega_B = 2\pi c/\lambda_B$ . When the refractive index of the Bragg grating layers is modulated in time, the system transforms from a passive filter into an active, time-variant medium capable of parametric amplification in transmission. Consider the temporal Bragg grating in Fig. 1, where either the high-index or low-index layers experience sinusoidal temporal modulation:

$$n(x, t) = \begin{cases} n_H(t) = n_{H,av} + \Delta_H \cos(\omega_m t + \phi_H) \\ n_L(t) = n_{L,av} + \Delta_L \cos(\omega_m t + \phi_L), \end{cases} \quad (1)$$

where  $\Delta_H = \delta_H n_H$  and  $\Delta_L = \delta_L n_L$ , in which  $\delta_H$  and  $\delta_L$  are the temporal modulation amplitudes of the high and low index layers, respectively. In addition,  $\omega_m = 2\pi f_m$  is the modulation frequency,  $\delta_H, \delta_L \ll n_{av}$  are the modulation depths, and  $\phi_H, \phi_L$  are modulation phases. The temporal Bragg grating consists of  $N$  periods, each with spatial period  $\Lambda$ . The total physical length of the structure is:

$$L = N\Lambda = N(d_H + d_L), \quad (2)$$

where  $d_H = \lambda_B/(4n_H)$  and  $d_L = \lambda_B/(4n_L)$  are the thicknesses of the high- and low-index layers, respectively. This length  $L$  determines the interaction distance for parametric processes and appears in all phase-matching conditions and gain expressions. This temporal variation breaks time-translation symmetry, enabling energy transfer from the modulation pump at frequency  $\omega_m$  to the optical signal at  $\omega_0$  via parametric photon conversion

$$\hbar\omega_{\text{out}} = \hbar\omega_0 \pm \hbar\omega_m. \quad (3)$$

### B. Constructive Interference of Multi-Harmonic Scattering

The amplification mechanism in temporal Bragg gratings can be visualized as a distributed multi-harmonic scattering process, where the input wave at frequency  $\omega_0$  interacts with time-modulated interfaces to generate sidebands at  $\omega_{\pm 1} = \omega_0 \pm \omega_m$ , as illustrated in Fig. 2. These harmonics undergo multiple reflections and transmissions throughout the structure, with constructive interference selectively enhancing the fundamental frequency  $\omega_0$ .

Consider a temporal Bragg grating composed of  $N$  alternating layers with time-varying refractive indices  $n_j(t) = n_{j,0} + \delta n_j \cos(\omega_m t + \phi_j)$ . At each interface  $j$  between layers  $j$  and  $j+1$ , the time-varying Fresnel coefficients couple different temporal harmonics. For a monochromatic wave at frequency  $\omega_p = \omega_0 + p\omega_m$ , the standard scattering matrix at interface  $j$  reads

$$\mathbf{S}_p^{(j)} = \begin{pmatrix} r_p^{(j)} & t_p^{(j)} \\ t_p^{(j)} & -r_p^{(j)} \end{pmatrix}, \quad (4)$$

where the Fresnel coefficients are:

$$r_p^{(j)} = \frac{n_j(\omega_p) - n_{j+1}(\omega_p)}{n_j(\omega_p) + n_{j+1}(\omega_p)}, \quad t_p^{(j)} = \frac{2n_j(\omega_p)}{n_j(\omega_p) + n_{j+1}(\omega_p)}. \quad (5)$$

Due to temporal modulation, the refractive indices become time-dependent, introducing coupling between harmonics. Expanding the time-varying Fresnel coefficients to first order in  $\delta n_j$

$$\begin{aligned} r^{(j)}(t) &= r_0^{(j)} + \frac{\delta n_j}{2} \left( \frac{\partial r^{(j)}}{\partial n_j} e^{i\omega_m t} + \frac{\partial r^{(j)}}{\partial n_{j+1}} e^{i\omega_m t} \right) + \text{c.c.}, \\ t^{(j)}(t) &= t_0^{(j)} + \frac{\delta n_j}{2} \left( \frac{\partial t^{(j)}}{\partial n_j} e^{i\omega_m t} + \frac{\partial t^{(j)}}{\partial n_{j+1}} e^{i\omega_m t} \right) + \text{c.c..} \end{aligned} \quad (6)$$

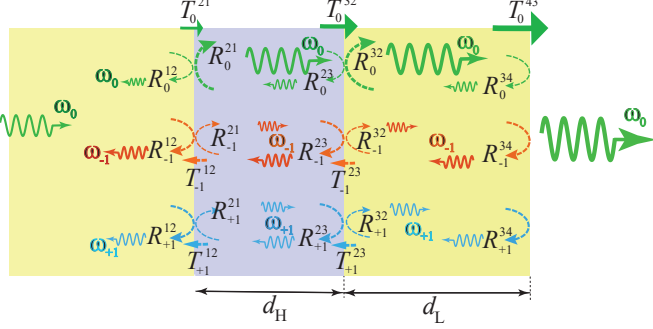


Fig. 2. Amplification of  $\omega_0$  arises from multiple reflections and transmissions of the main frequency  $\omega_0$  and generated sidebands  $\omega_{\pm 1} = \omega_0 \pm \omega_m$  through time-modulated layers. While  $\omega_{\pm 1}$  are generated via parametric coupling at each interface, only  $\omega_0$  experiences constructive interference across the structure, leading to net gain in transmission.

This temporal variation generates a block scattering matrix that couples harmonics  $p$  and  $q$ :

$$\underline{\mathbf{S}}^{(j)} = \begin{pmatrix} \ddots & \vdots & \vdots & \vdots & \vdots \\ \cdots & \mathbf{S}_{0,0}^{(j)} & \mathbf{S}_{0,+1}^{(j)} & \mathbf{S}_{0,-1}^{(j)} & \cdots \\ \cdots & \mathbf{S}_{+1,0}^{(j)} & \mathbf{S}_{+1,+1}^{(j)} & \mathbf{S}_{+1,-1}^{(j)} & \cdots \\ \cdots & \mathbf{S}_{-1,0}^{(j)} & \mathbf{S}_{-1,+1}^{(j)} & \mathbf{S}_{-1,-1}^{(j)} & \cdots \\ \vdots & \vdots & \vdots & \vdots & \vdots \end{pmatrix}, \quad (7)$$

where the diagonal blocks  $\mathbf{S}_{p,p}^{(j)}$  are given by Eq. (4) and the off-diagonal coupling blocks are:

$$\mathbf{S}_{p,q}^{(j)} = \frac{\delta n_j}{2n_0} \begin{pmatrix} \Delta r_{pq}^{(j)} & \Delta t_{pq}^{(j)} \\ \Delta t_{pq}^{(j)} & -\Delta r_{pq}^{(j)} \end{pmatrix}, \quad |p - q| = 1, \quad (8)$$

where the coupling coefficients  $\Delta r_{pq}^{(j)}$  and  $\Delta t_{pq}^{(j)}$  derive from the derivatives in Eq. (6). For a grating with  $N$  interfaces, the total scattering matrix is obtained by cascading individual matrices using the Redheffer star product  $\star$ :

$$\underline{\mathbf{S}}_{\text{total}} = \underline{\mathbf{S}}^{(1)} \star \underline{\mathbf{S}}^{(2)} \star \cdots \star \underline{\mathbf{S}}^{(N)}. \quad (9)$$

Define the harmonic amplitude vectors for forward ( $\mathbf{F}^{(j)}$ ) and backward ( $\mathbf{B}^{(j)}$ ) waves in layer  $j$

$$\mathbf{F}^{(j)} = [\dots, F_{-1}^{(j)}, F_0^{(j)}, F_{+1}^{(j)}, \dots]^T, \quad (10a)$$

$$\mathbf{B}^{(j)} = [\dots, B_{-1}^{(j)}, B_0^{(j)}, B_{+1}^{(j)}, \dots]^T. \quad (10b)$$

The scattering relation for the entire structure is:

$$\begin{pmatrix} \mathbf{B}^{(1)} \\ \mathbf{F}^{(N+1)} \end{pmatrix} = \underline{\mathbf{S}}_{\text{total}} \begin{pmatrix} \mathbf{F}^{(1)} \\ \mathbf{B}^{(N+1)} \end{pmatrix}. \quad (11)$$

From the scattering picture emerges a set of coupled amplitude equations that explicitly track the multiple reflection paths shown in Fig. 2. For harmonic  $p$  in layer  $j$ :

$$A_p^{(j)} = t_p^{(j-1)} A_p^{(j-1)} + r_p^{(j)} A_p^{(j+1)} + \sum_{q=p\pm 1} \left[ \kappa_{pq}^{(j)} A_q^{(j-1)} + \kappa_{pq}^{(j)} A_q^{(j+1)} \right], \quad (12a)$$

$$\kappa_{pq}^{(j)} = \frac{\delta n_j}{2n_0} \frac{\partial t^{(j)}}{\partial n} e^{i(\phi_j + \beta_q d_j)}, \quad (12b)$$

where  $\beta_q = n_{\text{eff},q} \omega_q / c$  is the propagation constant for harmonic  $q$ , and  $d_j$  is the thickness of layer  $j$ . The different interference conditions for  $\omega_0$  versus  $\omega_{\pm 1}$  explain the observed selective amplification.

*Amplification of  $\omega_0$*  The multiple reflection paths for  $\omega_0$  add coherently when the round-trip phase accumulation satisfies

$$2 \sum_{j=1}^N \beta_0^{(j)} d_j + \arg \left( r_0^{(j)} r_0^{(j+1)} \right) = 2\pi m, \quad m \in \mathbb{Z}, \quad (13)$$

and parametric contributions from  $\omega_{\pm 1}$  via coupling terms  $\kappa_{0,\pm 1}$  arrive in phase, leading to constructive interference and exponential growth.

*Suppression of  $\omega_{\pm 1}$* : The generated sidebands originate at different interfaces with phases

$$\phi_{\pm 1}^{(j)} = \phi_j \pm \omega_m t_j, \quad (14)$$

where  $t_j$  is the arrival time at interface  $j$ . These phase variations prevent coherent buildup, resulting in:

$$A_{\pm 1}^{\text{total}} = \sum_{j=1}^N \kappa_{\pm 1,0}^{(j)} A_0^{(j)} e^{i\phi_{\pm 1}^{(j)}} \approx 0 \quad (\text{incoherent sum}). \quad (15)$$

The amplification can be understood as an effective Fabry-Perot resonance with parametrically enhanced reflectivity. Summing the geometric series of all reflection paths yields

$$R_{\text{eff}} = R_0 + \frac{|\kappa_{0,+1}|^2}{1 - R_{+1}} + \frac{|\kappa_{0,-1}|^2}{1 - R_{-1}}, \quad (16)$$

where  $R_p$  is the reflection coefficient for harmonic  $p$ . The total power gain for  $\omega_0$  is then

$$G_{\text{total}} = \left| \frac{t_0^{(\text{in})} t_0^{(\text{out})}}{1 - R_{\text{eff}} e^{i\Phi}} \right|^2, \quad (17)$$

with  $\Phi = 2\beta_0 L$  being the round-trip phase. This multi-harmonic scattering formulation reveals three key insights.

- **Distributed parametric coupling:** Each time-modulated interface acts as a three-wave mixer, generating sidebands  $\omega_{\pm 1}$  from  $\omega_0$ .
- **Coherent path interference:** Multiple reflection paths for  $\omega_0$  interfere constructively when the Bragg condition and parametric phase-matching are simultaneously satisfied.
- **Harmonic-dependent interference:** Sidebands  $\omega_{\pm 1}$  experience destructive interference due to phase variations, acting primarily as intermediate states for energy transfer to  $\omega_0$ .

This picture explains why temporal Bragg gratings function as *through-port* amplifiers: the amplified  $\omega_0$  emerges in transmission after coherent buildup through the structure, while the generated sidebands remain weak due to incoherent summation.

### C. Maxwell's Equations

Consider a temporal Bragg grating with refractive index modulation

$$n(\mathbf{r}, t) = n_0(\mathbf{r}) + \delta n(\mathbf{r}) \cos(\omega_m t + \phi(\mathbf{r})), \quad (18)$$

where  $\delta n \ll n_0$ ,  $\omega_m$  is the modulation frequency, and the modulation is applied selectively to either high-index ( $n_H$ ) or low-index ( $n_L$ ) layers. For a non-magnetic, lossless dielectric medium with time-varying refractive index, Maxwell's equations read

$$\nabla \times \mathbf{E} = -\mu_0 \frac{\partial \mathbf{H}}{\partial t}, \quad (19a)$$

$$\nabla \times \mathbf{H} = \epsilon_0 \frac{\partial}{\partial t} [n^2(\mathbf{r}, t) \mathbf{E}]. \quad (19b)$$

The time derivative of the displacement field becomes:

$$\begin{aligned} \frac{\partial \mathbf{D}}{\partial t} &= \epsilon_0 \frac{\partial}{\partial t} [n^2(\mathbf{r}, t) \mathbf{E}] \\ &= \epsilon_0 \left[ n^2(\mathbf{r}, t) \frac{\partial \mathbf{E}}{\partial t} + 2n(\mathbf{r}, t) \frac{\partial n(\mathbf{r}, t)}{\partial t} \mathbf{E} \right], \end{aligned} \quad (20a)$$

where for small modulation depth ( $\delta n \ll n_0$ )

$$n^2(\mathbf{r}, t) \approx n_0^2(\mathbf{r}) + 2n_0(\mathbf{r})\delta n(\mathbf{r}) \cos(\omega_m t) \quad (20b)$$

$$\frac{\partial n^2}{\partial t} \approx -2n_0(\mathbf{r})\delta n(\mathbf{r})\omega_m \sin(\omega_m t). \quad (20c)$$

Considering a  $z$ -polarized wave propagating in the  $x$ -direction in a one-dimensional structure, combining Maxwell's equations yields

$$\frac{\partial^2 E_z}{\partial x^2} - \frac{n^2(x, t)}{c^2} \frac{\partial^2 E_z}{\partial t^2} - \frac{1}{c^2} \frac{\partial n^2}{\partial t} \frac{\partial E_z}{\partial t} = 0. \quad (20d)$$

The structure has dual periodicity: spatial period  $\Lambda$  (Bragg period) and temporal period  $T_m = 2\pi/\omega_m$ . According to Floquet-Bloch theorem, solutions take the form

$$E_z(x, t) = e^{j(\beta x - \omega_0 t)} \sum_{p=-\infty}^{\infty} \sum_{q=-\infty}^{\infty} A_{pq} e^{j(pKx + q\omega_m t)}, \quad (21a)$$

where  $\beta$  is the Bloch wavevector,  $K = 2\pi/\Lambda$  is the grating wavevector, and  $A_{pq}$  are the amplitudes of spatial harmonic  $p$  and temporal harmonic  $q$ . For practical analysis considering only temporal harmonics (setting spatial harmonics  $p = 0$  for the fundamental mode), the field expands as

$$E_z(x, t) = \sum_{p=-\infty}^{\infty} \left[ A_p^+(x) e^{j(\beta_p x - \omega_p t)} + A_p^-(x) e^{j(-\beta_p x - \omega_p t)} \right], \quad (21b)$$

where  $\omega_p = \omega_0 + p\omega_m$ ,  $\beta_p = n_{\text{eff}}(\omega_p)\omega_p/c$ , and  $n_{\text{eff}}$  is the effective index of the guided mode.

Applying the slowly varying envelope approximation to Maxwell's equations yields coupled-mode equations. For forward-propagating waves:

$$\begin{aligned} \frac{dA_p^+}{dx} &= -j\kappa_p A_p^- e^{-j2\Delta_p x} \\ &- j\frac{\omega_p}{c} \delta n(x) \sum_{q \neq p} C_{pq} A_q^+ e^{-j\Delta k_{pq} x}, \end{aligned} \quad (22a)$$

and for backward-propagating waves

$$\begin{aligned} \frac{dA_p^-}{dx} &= +j\kappa_p A_p^+ e^{+j2\Delta_p x} \\ &+ j\frac{\omega_p}{c} \delta n(x) \sum_{q \neq p} C_{pq} A_q^- e^{-j\Delta k_{pq} x}, \end{aligned} \quad (22b)$$

where  $\kappa_p$  is the spatial coupling coefficient due to Bragg periodicity,  $\Delta_p = \beta_p - \pi/\Lambda$  is detuning from the Bragg condition, and

$$\Delta k_{pq} = \beta_p - \beta_q - (p - q)K, \quad (23)$$

is the phase mismatch between harmonics  $p$  and  $q$ . The coupling coefficients are determined by overlap integrals

$$C_{pq} = \frac{\int_{\text{modulated layers}} E_p^*(x) E_q(x) dx}{\sqrt{\int_{\text{structure}} |E_p(x)|^2 dx \int_{\text{structure}} |E_q(x)|^2 dx}}. \quad (24)$$

#### D. Parametric Amplification Mechanism

For parametric amplification, we consider three interacting waves: pump ( $\omega_m$ ), signal ( $\omega_s$ ), and idler ( $\omega_i$ ), with energy conservation  $\omega_s + \omega_i = \omega_m$  (for non-degenerate case) or  $\omega_s = \omega_i = \omega_m/2$  (for degenerate case). The coupled equations simplify to

$$\frac{dA_s}{dx} = -j\gamma A_i^* e^{-j\Delta k_{si} x}, \quad (25a)$$

$$\frac{dA_i}{dx} = -j\gamma A_s^* e^{-j\Delta k_{si} x}, \quad (25b)$$

where  $\gamma = \frac{\omega_s \delta n}{2c} \eta_{\text{overlap}}$  is the nonlinear coupling coefficient,  $\eta_{\text{overlap}}$  is the spatial overlap factor from Eq. (24), and  $\Delta k_{si} = \beta_s + \beta_i - \beta_m - K$  is the phase mismatch. When phase-matched ( $\Delta k_{si} = 0$ ), the solution exhibits exponential growth

$$A_s(x) = A_s(0) \cosh(gx) + jA_i^*(0) \sinh(gx), \quad (26a)$$

$$A_i(x) = A_i(0) \cosh(gx) + jA_s^*(0) \sinh(gx), \quad (26b)$$

with parametric gain coefficient

$$g = |\gamma| = \left| \frac{\omega_s \delta n}{2c} \cdot \eta_{\text{overlap}} \right|. \quad (27a)$$

The power gain in decibels after propagation through a structure of length  $L$  is

$$\begin{aligned} G_{\text{dB}} &= 10 \log_{10} [\cosh^2(gL)] \\ &\approx \begin{cases} 4.343(gL)^2 & \text{for } gL \ll 1 \\ 8.686gL - 6.020 & \text{for } gL \gg 1. \end{cases} \end{aligned} \quad (27b)$$

*Layer-Dependent Asymmetric Gain:* The spatial overlap factor  $\eta_{\text{overlap}}$  differs significantly depending on whether modulation is applied to high-index or low-index layers. For high-index layer modulation

$$\eta_{\text{overlap}}^H \approx \frac{\int_{\text{high-index layers}} |E(x)|^2 dx}{\int_{\text{all layers}} |E(x)|^2 dx} > \frac{1}{2}, \quad (28a)$$

since the field concentrates in high-index layers in a quarter-wave stack. For low-index layer modulation:

$$\eta_{\text{overlap}}^L \approx \frac{\int_{\text{low-index layers}} |E(x)|^2 dx}{\int_{\text{all layers}} |E(x)|^2 dx} < \frac{1}{2}. \quad (28b)$$

This asymmetry in field overlap leads to different gain spectra: high-index modulation preferentially amplifies frequencies above  $\omega_0$ , while low-index modulation amplifies frequencies below  $\omega_0$ . The gain asymmetry ratio reads

$$\frac{G(\omega_0 + \Delta\omega)}{G(\omega_0 - \Delta\omega)} \approx \left( \frac{\eta_{\text{overlap}}^H(\omega_0 + \Delta\omega)}{\eta_{\text{overlap}}^L(\omega_0 - \Delta\omega)} \right)^2. \quad (28c)$$

### E. Resonant Modulation Conditions

*Degenerate Parametric Amplification:* When the modulation frequency equals the Bragg frequency ( $\omega_m = \omega_B$ ), the system operates in degenerate mode with  $\omega_s = \omega_i = \omega_B/2$ . The gain is enhanced by the cavity quality factor  $Q$

$$g_{\text{deg}} = \frac{\omega_0 \delta n}{4c} \cdot \eta_{\text{overlap}} \cdot Q, \quad (29)$$

where  $Q = \omega_B/\Delta\omega_{\text{FWHM}}$  characterizes the Bragg resonance linewidth.

*Subharmonic Resonance:* For  $\omega_m = 2\omega_B$ , the signal and idler are at  $\omega_B$ , creating a second-harmonic-type process. The phase-matching condition is given by

$$\Delta k = 2\beta(\omega_B) - \beta(2\omega_B) - K = 0. \quad (30)$$

This condition can be satisfied near the photonic band edge where dispersion is strong.

*Optimal Gain Condition:* The maximum gain occurs near  $\omega_m = 1.5\omega_B$ . This corresponds to signal and idler frequencies  $\omega_s = 0.5\omega_m = 0.75\omega_B$  and  $\omega_i = 0.5\omega_m = 0.75\omega_B$ , placing both near the band edge where group velocity is minimal and interaction time is maximized.

## III. RESULTS

### A. Regime I: Coherent and Supra-Bragg Modulation

Figure 3 illustrates power amplification in a coherent temporal Bragg grating when the modulation frequency  $\omega_m$  is equal to the Bragg frequency  $\omega_B = 300$  THz, corresponding to a central wavelength  $\lambda_B = 1\mu\text{m}$ . The electric field distributions reveal distinct spectral behaviors. At 150 THz ( $\omega_B/2$ ), the field pattern shows clear amplification (Fig. 3(a)). At 300 THz ( $\omega_B$ ), strong reflection is observed with no transmission, as expected at the main Bragg frequency (Fig. 3(b)). At 450 THz ( $1.5\omega_B$ ), significant field amplification reappears (Fig. 3(c)). The transmission spectrum (Fig. 3(d)) further confirms that when the high-index layers are static ( $\delta_H = 0$ ) and the low-index layers are time-modulated ( $\delta_L > 0$ ), substantial gain occurs at frequencies symmetrically displaced from  $\omega_B$ , notably at  $\omega_B/2$  and  $1.5\omega_B$ , while transmission is suppressed at the Bragg frequency itself. These results demonstrate that a coherent temporal modulation at the Bragg frequency enables parametric amplification at sub- and super-harmonic frequencies which effectively converts static photonic bandgaps into gain bands at detuned frequencies.

Figure 4 presents the time-averaged power flow and electromagnetic energy density distribution within the coherent temporal Bragg grating from Figure 3, analyzed at the three characteristic frequencies: the amplification band at 150 THz ( $\omega_B/2$ ), the reflection band at 300 THz ( $\omega_B$ ), and the second amplification band at 450 THz ( $1.5\omega_B$ ). At 150 THz (Fig. 4(a)): The power flow profile shows a significant net positive flux that grows along the propagation direction. This monotonic increase is a direct signature of distributed parametric amplification occurring throughout the grating, consistent with the field amplification seen in Fig. 3(a). Energy is being added to the wave via the temporal modulation of the low-index layers. At 300 THz (Fig. 4(b)): The power flow exhibits

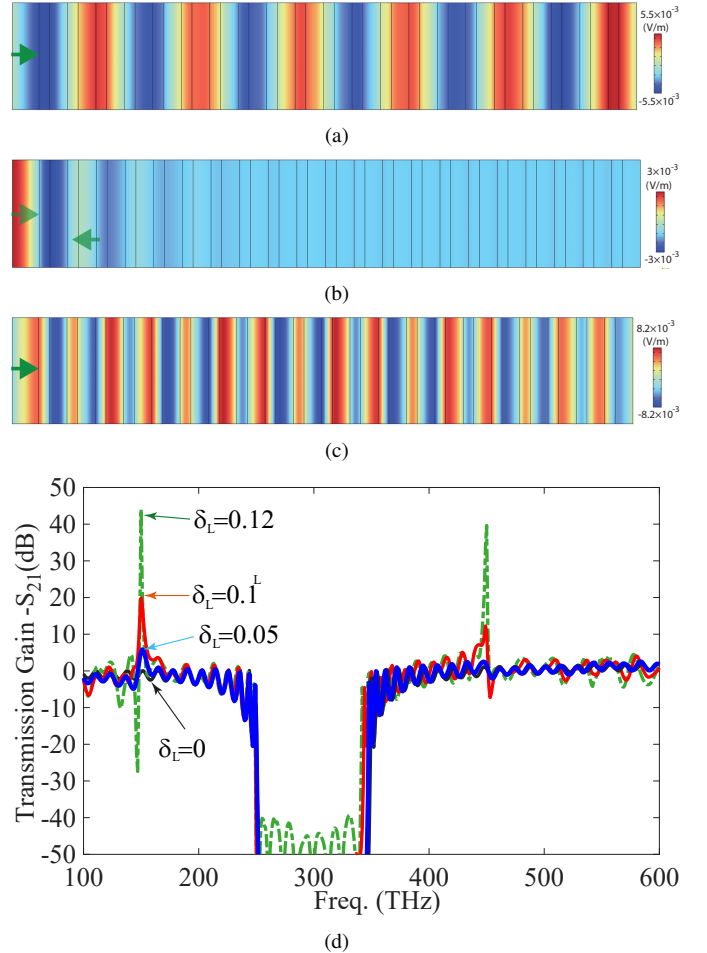


Fig. 3. Power amplification in a coherent temporal Bragg grating with a modulation frequency equal to the Bragg frequency,  $\omega_m = \omega_B = 300$  THz. The structure parameters are  $n_L = 1.5$ ,  $n_H = 2.5$ ,  $\lambda_0 = 1\mu\text{m}$ ,  $\Lambda = 20$ ,  $\delta_H = 0$ , and  $\delta_L = 0.12$ . (a)-(c) Normal electric field distribution at 150 THz ( $= \omega_B/2$ ), 300 THz ( $= \omega_B$ ), and 450 THz ( $= 1.5\omega_B$ ), respectively. (d) Transmission gain for different time-periodic low-index modulations  $\delta_L > 0$ , with static high-index layers ( $\delta_H = 0$ ).

a characteristic standing-wave pattern with a vanishing net flux. The flow oscillates between positive and negative values, indicating strong backward reflection and interference between incident and reflected waves. This confirms the existence of a photonic bandgap at the central Bragg frequency  $\omega_B$ , where transmission is inhibited. At 450 THz (Fig. 4(c)): Similar to the 150 THz case, the power flow demonstrates a clear amplifying trend, increasing with propagation distance. This confirms that the gain mechanism is active not only at the sub-harmonic ( $\omega_B/2$ ) but also at a super-harmonic ( $1.5\omega_B$ ) frequency, highlighting the frequency-symmetric nature of the parametric process driven by modulation at  $\omega_m = \omega_B$ .

The electromagnetic energy density at 150 and 450 THz (Figs. 4(d) and 4(f)) shows a pronounced and growing concentration within the time-modulated low-index layers (corresponding to the regions with  $\delta_L > 0$ ). This spatial localization and growth of energy directly correlate with the zones of active power injection, visualizing how the temporal modulation pumps energy into the system at these detuned

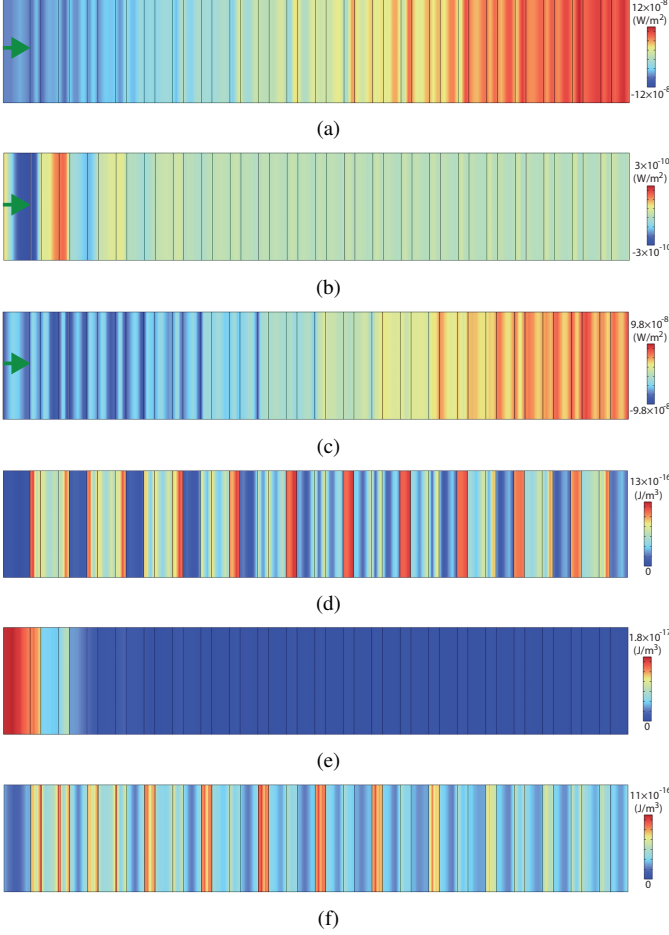


Fig. 4. Time-averaged power flow and energy distribution in the Bragg grating in Fig. 3. (a)-(c) Power flow at frequencies 150, 300 and 450 THz, respectively. (d)-(f) Energy density at 150, 300 and 450 THz, respectively.

frequencies. At 300 THz (Fig. 4(e)), the energy density forms a stationary, high-contrast interference pattern typical of a Bragg reflector. The energy is largely confined and does not propagate, reinforcing the bandgap behavior observed in the power flow. The distribution is static, with no net growth along the structure.

The results in Fig. 4 provide a complete spatial-energy picture of the coherent temporal grating's operation. They visually corroborate the transmission spectrum from Fig. 3(d) by showing i) Amplification Bands: Net growing power flow and concurrent energy buildup in the modulated layers at frequencies detuned from  $\omega_B$  (150 THz and 450 THz). ii) Photonic Bandgap: Resonant reflection with zero net power flow and a stationary energy pattern at the Bragg frequency (300 THz). This analysis confirms that a temporal modulation at the Bragg frequency  $\omega_m = \omega_B$  fundamentally transforms a static photonic crystal from a passive reflector into an active, distributed parametric amplifier for frequencies outside the original bandgap, while preserving perfect reflection at the central frequency.

Figure 5 examines the impact of modulating the high-index layers on power amplification in a coherent temporal Bragg grating, under the condition  $\omega_m = \omega_B = 300$  THz.

The parameters are the same as in Fig. 3, but with a key modification: the low-index layers are now static ( $\delta_L = 0$ ), while the high-index layers undergo time-periodic modulation with varying amplitudes  $\delta_H > 0$ . An additional case with concurrent modulations ( $\delta_L = 0.06$ ,  $\delta_H = 0.036$ ) is also shown.

The spectra for high-index layer modulation ( $\delta_L = 0$ ,  $\delta_H > 0$ ) confirm that amplification persists at the same characteristic frequencies of 150 THz ( $= \omega_B/2$ ) and 450 THz ( $= 1.5\omega_B$ ), demonstrating that the parametric gain mechanism is not exclusive to low-index modulation. The gain magnitude increases significantly with larger modulation amplitudes  $\delta_H$ . For instance, the gain at both 150 THz and 450 THz for  $\delta_H = 0.08$  exceeds 60 dB, substantially higher than the gains observed in Fig. 5 for comparable  $\delta_L$  values. This indicates that modulating the high-index layers can be a more efficient method for generating parametric amplification in this structure. The reflection bandgap at the central Bragg frequency (300 THz) remains intact, maintaining near-zero transmission. The curve for concurrent modulation case ( $\delta_L = 0.06$ ,  $\delta_H = 0.036$ ) in Fig. 5 shows a remarkable gain profile for such small modulation strengths. The achieved amplification is lower than for the largest pure  $\delta_H = 0.08$  modulations but demonstrates that the effect is the same when both layers are weakly modulated. This suggests that the total modulation strength and its distribution influence the final gain. The gain does not simply result from adding the effects of individual modulations; it depends on their relative phases and amplitudes within the grating's temporal dynamics.

The results in Fig. 5 reveal that time-varying high-index layers are highly effective for generating parametric amplification in a coherent temporal Bragg grating. The gain mechanism remains frequency-symmetric around  $\omega_B$ , producing strong amplification at  $\omega_B/2$  and  $1.5\omega_B$ . Crucially, modulating the high-index layers can yield substantially higher gain compared to modulating the low-index layers for similar modulation depths, highlighting the importance of the modulation's location within the periodic structure. This flexibility in choosing the modulated component (high-index, low-index, or both) provides an additional degree of freedom for designing and optimizing active photonic devices based on temporal bandgap engineering.

Figure 6 demonstrates frequency-agile parametric amplification in a temporal Bragg grating, achieved by decoupling the modulation frequency  $\omega_m$  from the Bragg frequency  $\omega_B$ . Here, the system parameters remain the same as in Fig. 3, except that the modulation frequency is varied relative to  $\omega_B$ . The results show that the amplification peaks are not fixed at  $\omega_B/2$  and  $1.5\omega_B$ , but instead shift dynamically with  $\omega_m$ , enabling tunable gain across a broad spectral range. The figure clearly illustrates that the amplification frequency is directly controlled by the modulation frequency  $\omega_m$ . Each curve corresponds to a different modulation frequency, expressed as a fraction or multiple of  $\omega_B$ , where for  $\omega_m = 0.8\omega_B$ , the peak amplification occurs at  $f = 120$  THz, for  $\omega_m = 0.9\omega_B$ , the peak shifts to  $f = 135$  THz, for  $\omega_m = 1.2\omega_B$ , amplification is observed at  $f = 180$  THz, for  $\omega_m = 1.4\omega_B$ , the peak moves to  $f = 210$  THz, and for  $\omega_m = 1.5\omega_B$ , amplification occurs at

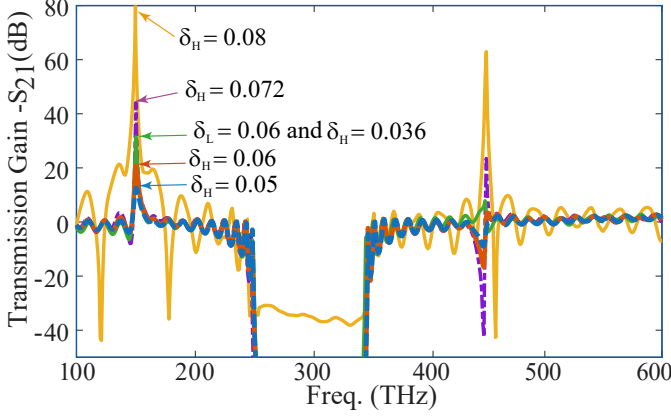


Fig. 5. Power amplification in a coherent temporal Bragg grating with modulation frequency  $\omega_m = \omega_B$ . Spectra are shown for the case where the low-index layers are static ( $\delta_L = 0$ ) and the high-index layers are time-modulated with varying amplitudes  $\delta_H$ , along with one case of concurrent modulation ( $\delta_L = 0.06, \delta_H = 0.036$ ). All other parameters match those in Fig. 2. The plot demonstrates strong parametric gain at  $f = 150$  THz =  $\omega_B/2$  and  $450$  THz =  $1.5\omega_B$ .

$$f = 225 \text{ THz.}$$

This linear relationship confirms that the gain mechanism is parametric in nature, where the amplified frequencies are determined by phase-matching conditions between the pump (modulation) and the signal/idler waves. Specifically, amplification arises at frequencies satisfying  $\omega_{\text{signal}} = \omega_B \pm \omega_m$ , or through higher-order processes. The observed peaks correspond to the Stokes and anti-Stokes sidebands generated by the temporal modulation of the grating's refractive index. Key implications are as follows.

- Tunability: By simply adjusting the modulation frequency  $\omega_m$ , the amplification band can be continuously tuned across a wide frequency range. This provides a powerful degree of freedom for designing reconfigurable optical amplifiers and frequency converters.
- Beyond Coherent Modulation: Unlike the coherent case ( $\omega_m = \omega_B$ ), where gain is symmetrically localized at  $\omega_B/2$  and  $1.5\omega_B$ , detuning the modulation breaks this symmetry. The amplification becomes asymmetric and can be placed at desired frequencies relative to the Bragg bandgap.
- Preservation of the Bandgap: Despite the shift in amplification peaks, the original photonic bandgap around  $\omega_B = 300$  THz remains largely intact, as evidenced by the persistent reflection dip near that frequency in all curves. This indicates that the temporal modulation primarily affects frequencies outside the static bandgap, enabling simultaneous reflection at one frequency and amplification at another.

The results in Fig. 6 establish that a temporal Bragg grating functions as a frequency-agile parametric amplifier, where the gain spectrum can be dynamically reconfigured by varying the modulation frequency. This tunability, combined with the structure's inherent bandgap properties, makes it a promising platform for multifunctional photonic devices that require simultaneous frequency-selective amplification, filtering, and

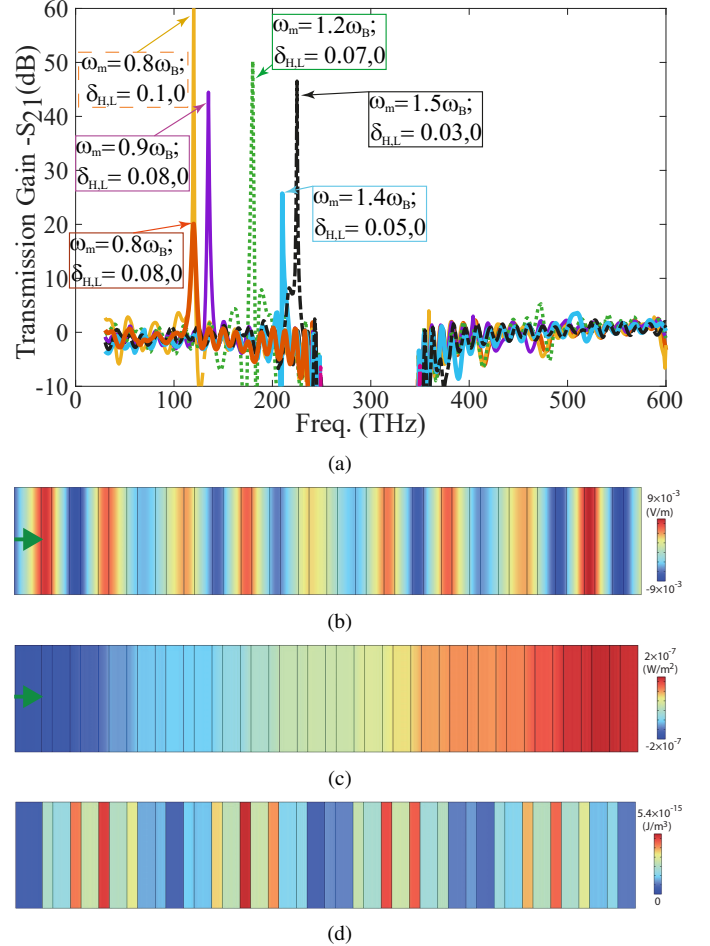


Fig. 6. Frequency-agile power amplification in a temporal Bragg grating with the same parameters as in Fig. 3, except for distinct modulation frequencies of  $\omega_m = \omega_B \times [0.8, 0.9, 1.2, 1.4, 1.5]$  corresponding to distinct peak amplification frequencies of  $f = [120, 135, 180, 210, 225]$  THz.

signal processing in dynamically controlled optical systems.

### B. Regime II: Sub-Bragg Modulation

Figure 7 explores the regime of sub-Bragg modulation, where the modulation frequency is lower than the Bragg frequency ( $\omega_m < \omega_B$ ). The study reveals that achieving significant parametric amplification in this region requires substantially stronger modulation strengths compared to the supra-Bragg case ( $\omega_m > \omega_B$ ), highlighting an asymmetry in the system's nonlinear response. The transmission gain spectra in Fig. 7(a) show clear amplification peaks at frequencies directly tied to the modulation frequency:  $f = 45, 60, 75$ , and  $90$  THz for  $\omega_m = 0.3\omega_B, 0.4\omega_B, 0.5\omega_B$ , and  $0.6\omega_B$ , respectively. This confirms the frequency-agile nature of the gain. Crucially, to achieve gain levels on the order of tens of dB in this sub-Bragg regime, the modulation amplitudes must be set significantly higher ( $\delta_L = \delta_H = 0.1$ ) than those typically sufficient for the coherent ( $\omega_m = \omega_B$ ) or supra-Bragg cases shown in previous figures. This indicates a reduced parametric coupling efficiency when  $\omega_m < \omega_B$ .

The electric field and energy dynamics at  $f = 90$  THz in Figs. 7(b)-7(d) show that for the case  $\omega_m = 0.6\omega_B$  and

strong modulation ( $\delta_L = \delta_H = 0.1$ ), the spatial distributions at the amplification frequency (90 THz) provide insight into the operative physics. The normal electric field distribution in Fig. 7(b) shows a propagating wave with a growing envelope, characteristic of distributed amplification. The pattern confirms that efficient power transfer is occurring despite the sub-Bragg modulation condition. The time-averaged power flow in Fig. 7(c) exhibits a clear monotonic increase along the propagation direction. This positive, growing flux is the definitive signature of net power amplification supplied by the temporal modulation. The energy density in Fig. 7(d) confirms that the electromagnetic energy density is strongly localized and enhanced within the modulated layers of the grating. This spatial concentration of energy correlates directly with the zones of active power injection, visualizing how the strong modulation pumps energy into the system at the detuned frequency.

The need for stronger modulation in the sub-Bragg regime can be understood through the phase-matching condition and the photonic density of states near the bandgap. For  $\omega_m < \omega_B$ , the generated sidebands (e.g.,  $\omega_B \pm \omega_m$ ) lie closer to the center of the original photonic bandgap. The group velocity of waves near the gap edge is significantly reduced, leading to a longer interaction time but also a weaker coupling to the propagating modes due to the distorted dispersion relation. Therefore, a larger modulation depth (stronger perturbation) is required to achieve the same nonlinear coupling strength and gain compared to the supra-Bragg case, where sidebands fall in regions of higher group velocity and more favorable dispersion.

The results in Fig. 7 demonstrate that while frequency-agile amplification is achievable for  $\omega_m < \omega_B$ , it comes at the cost of requiring significantly higher modulation strengths. This reveals an important asymmetry in the parametric gain efficiency between the sub-Bragg and supra-Bragg regimes, governed by the underlying dispersion of the static photonic crystal. The strong field growth, increasing power flow, and localized energy density confirm that effective amplification is still possible, provided the modulation is sufficiently strong. This insight is crucial for designing practical tunable amplifiers, as it dictates different pump power requirements depending on the desired operational frequency band relative to the Bragg condition.

### C. Regime III: Extreme Sub-Bragg Modulation and the Emergence of Broadband Gain via Multi-Phase-Matching

Figure 8 investigates the extreme sub-Bragg modulation regime, where the modulation frequency is a small fraction of the Bragg frequency ( $\omega_m = 0.1\omega_B$  and  $0.2\omega_B$ ). This regime reveals a significant transition in the system's behavior: while discrete, frequency-specific amplification peaks persist, a new broadband gain continuum emerges at high frequencies ( $\gtrsim \omega_B$ ), particularly for the smallest modulation frequency ( $\omega_m = 0.1\omega_B$ ).

**Persistence of Discrete Amplification with Strong Modulation:** As shown in Fig. 8(a), discrete amplification peaks are still generated at frequencies directly linked to the modulation

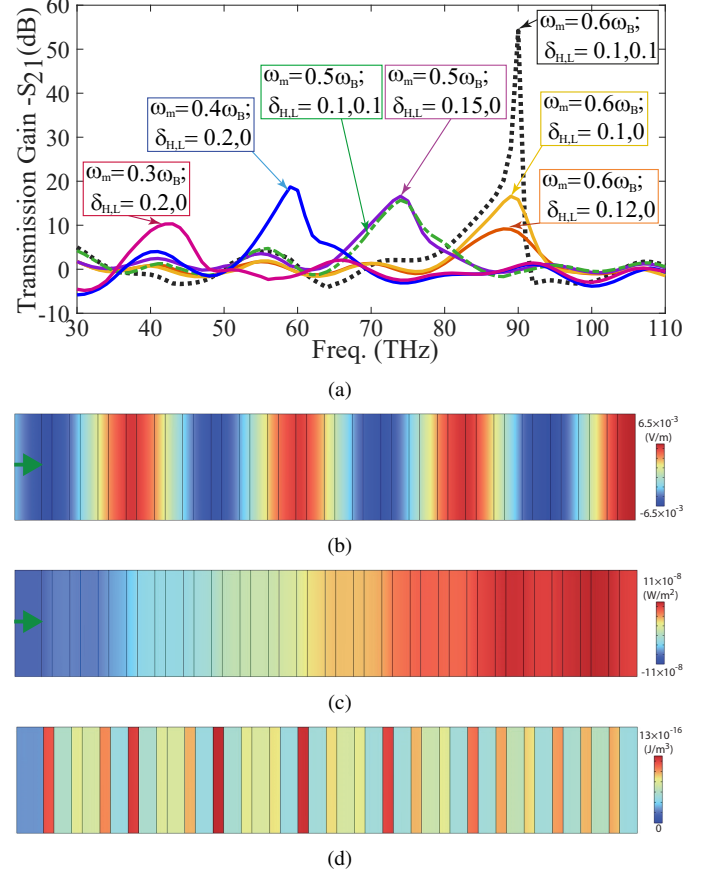


Fig. 7. Power amplification in the sub-Bragg modulation regime ( $\omega_m < \omega_B$ ). (a) Transmission gain spectra for modulation frequencies  $\omega_m = \omega_B \times [0.3, 0.4, 0.5, 0.6]$ , showing corresponding amplification peaks at  $f = [45, 60, 75, 90]$  THz. Significant gain in this regime requires strong modulation amplitudes ( $\delta_L = \delta_H = 0.1$ ). (b)-(d) Spatial distributions for the case  $\omega_m = 0.6\omega_B$  at its peak frequency  $f = 90$  THz: (b) normal electric field, (c) time-averaged power flow, and (d) electromagnetic energy density.

(e.g.,  $f \approx 12$  THz for  $\omega_m = 0.2\omega_B$  and  $f \approx 559$  THz for  $\omega_m = 0.1\omega_B$ ). Achieving substantial gain at these discrete peaks requires exceptionally strong modulation amplitudes ( $\delta_H = 0.2$  to  $0.4$ ), consistent with the reduced parametric coupling efficiency in the deep sub-Bragg regime.

The spatial distributions confirm the amplification physics for these discrete peaks: For the 12 THz peak ( $\omega_m = 0.2\omega_B$ , Fig. 8(b)-8(d)): The electric field (b) shows growth, the power flow (c) increases, and the energy density (d) localizes, confirming parametric gain. For the 559 THz peak ( $\omega_m = 0.1\omega_B$ , Fig. 8(e)-8(g)): Similar characteristics of field growth (e), positive power flux (f), and localized energy (g) are observed.

**Multi-Phase-Matching as the Origin of the Broadband High-Frequency Gain:** The most significant feature in Fig. 8(a) is the appearance of a broad, continuous band of gain at high frequencies. This broadband effect is not due to a single parametric process but results from multiple non-degenerate four-wave mixing processes that become simultaneously phase-matched when the modulation frequency  $\omega_m$  is very small.

Physically, for a small modulation wavenumber  $K = \omega_m n_g / c$ , the phase-matching condition for parametric ampli-

fication can be approximated as

$$\beta(\omega_0 + \Delta\omega) + \beta(\omega_0 - \Delta\omega) \approx 2\beta_0 + K, \quad (31)$$

where  $\beta_0 = \beta(\omega_0)$  is the propagation constant at the Bragg frequency. For a sufficiently small  $K$ , this condition can be satisfied for a continuous range of frequency detunings  $\Delta\omega$  within the system's phase-matching bandwidth  $\Delta\omega_{PM} \approx \pi c/(n_g L)$ , where  $L$  is the grating length and  $n_g$  the group index. Thus, as  $\omega_m \rightarrow 0$ , the modulation wavevector  $K$  becomes negligible compared to the dispersion scale. This allows a spectrum of signal-idler pairs around  $\omega_0$  to simultaneously satisfy the phase-matching condition, resulting in the observed broadband gain continuum rather than discrete sidebands.

*Conclusion and Design Implications:* The results in Fig. 8 demonstrate a fundamental operational transition in temporal Bragg gratings governed by the modulation frequency. For  $\omega_m \gtrsim 0.2\omega_B$ , the system operates as a discrete, frequency-agile parametric amplifier, where gain requires increasingly strong modulation as  $\omega_m$  decreases. For  $\omega_m \lesssim 0.1\omega_B$ , the system transitions to a broadband amplifier regime due to multi-phase-matching. Here, a single, low-frequency modulation pump can provide gain across a wide high-frequency band, limited primarily by the grating's dispersion and length. This insight provides the powerful design principle that the modulation frequency directly controls the gain bandwidth. Engineers can choose between narrowband, tunable amplification (using  $\omega_m \sim \omega_B$ ) and wideband, fixed-band amplification (using  $\omega_m \ll \omega_B$ ) by adjusting a single pump parameter, greatly enhancing the flexibility of temporally modulated photonic devices.

#### IV. CONCLUSION

We have introduced the concept of temporal Bragg gratings and have shown that they are capable of enabling efficient power amplification. A comprehensive investigation of power amplification in temporal Bragg gratings is conducted, exploring the effects of modulation location, frequency, and amplitude on the resulting gain spectrum and electromagnetic field dynamics. Our study demonstrates that temporal modulation fundamentally transforms a static photonic crystal from a passive filter into an active, reconfigurable amplifier, with performance governed by the interplay between spatial periodicity and temporal dynamics. The key findings are as follows.

- **Coherent Amplification:** When modulated at the Bragg frequency ( $\omega_m = \omega_B$ ), the grating provides strong parametric amplification at symmetrically displaced frequencies ( $\omega_B/2$  and  $1.5\omega_B$ ) while maintaining a reflection bandgap at the central frequency. This amplification is effective whether the high-index or low-index layers are modulated, with high-index modulation yielding higher gain for comparable depths.
- **Spectral Agility:** The amplification frequency is directly tunable by varying the modulation frequency  $\omega_m$ . This frequency-agile operation allows the gain peak to be placed at desired spectral locations ( $\omega_B \pm \omega_m$ ), enabling a single device to function as a tunable narrowband amplifier.

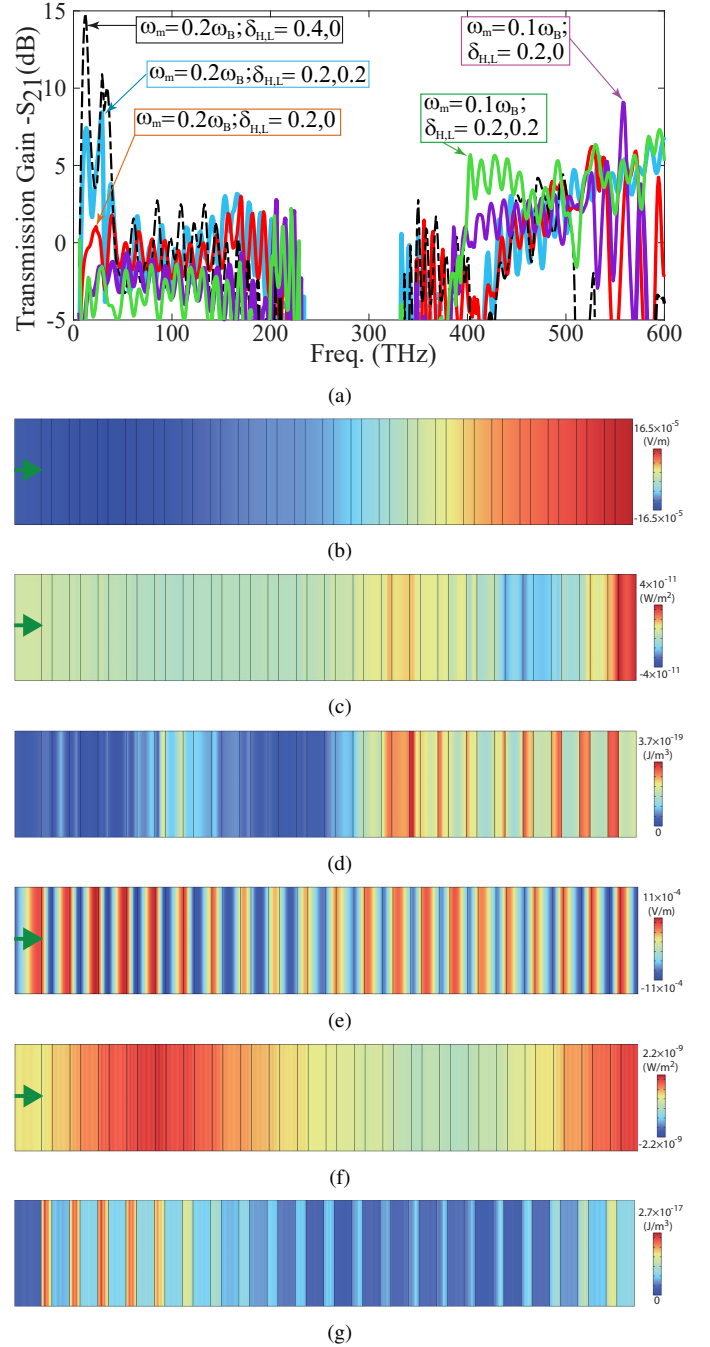


Fig. 8. Frequency-agile power amplification in a temporal Bragg grating with the same parameters as in Fig. 3, except for varying modulation amplitudes at distinct modulation frequencies of  $\omega_m = \omega_B \times [0.1, 0.2]$  corresponding to distinct peak amplification frequencies of  $f = [12, 559]$  THz. (a) Transmission gain. (b)-(d) Normal electric field distribution, time-average power flow, and energy density at  $f = 12$  THz for the grating with  $\omega_m = 0.2\omega_B$ ,  $\delta_H = 0.4$  and  $\delta_L = 0$ . (e)-(g) Normal electric field distribution, time-average power flow, and energy density at  $f = 559$  THz for the grating with  $\omega_m = 0.1\omega_B$ ,  $\delta_H = 0.2$  and  $\delta_L = 0$ .

- **Regime-Dependent Efficiency:** A marked asymmetry exists between the sub-Bragg ( $\omega_m < \omega_B$ ) and supra-Bragg ( $\omega_m > \omega_B$ ) regimes. Achieving significant gain in the sub-Bragg regime necessitates substantially stronger modulation, highlighting a design trade-off between operational frequency and required pump power.
- **Broadband Gain Transition:** For very low modulation frequencies ( $\omega_m \lesssim 0.1\omega_B$ ), the system transitions from discrete sideband amplification to a broadband gain continuum at high frequencies. This arises from multi-phase-matching, where a small modulation wavevector enables simultaneous amplification of a continuum of frequency pairs, effectively creating a wideband amplifier.

This work establishes temporal Bragg gratings as a versatile platform for active photonics, where a single structure can be dynamically reconfigured to perform as either a tunable narrowband amplifier or a broadband gain medium. This programmability, achieved by controlling a single parameter—the modulation frequency—opens new avenues for integrated, multifunctional photonic devices such as reconfigurable optical amplifiers, agile frequency converters, and enhanced light sources. Future explorations may extend this framework to disordered or aperiodic temporal modulations, investigate the role of nonlinearities and losses, and harness these principles for quantum optical applications, further solidifying the role of time as a fundamental new dimension in photonic engineering.

## REFERENCES

- [1] A. Othonos, “Fiber Bragg gratings,” *Rev. Sci. Instrum.*, vol. 68, no. 12, pp. 4309–4341, 1997.
- [2] K. O. Hill and G. Meltz, “Fiber Bragg grating technology fundamentals and overview,” *J. Light. Technol.*, vol. 15, no. 8, pp. 1263–1276, 2002.
- [3] N. Ansari, E. Mohebbi, and K. Fallah, “Ultra-broadband and broad-angle absorbers with transition metal dichalcogenide monolayer using thue–morse quasi-photonic crystals,” *Opt. Mater.*, vol. 107, p. 110039, 2020.
- [4] S. Taravati and G. V. Eleftheriades, “Full-duplex reflective beamsteering metasurface featuring magnetless nonreciprocal amplification,” *Nat. Commun.*, vol. 14, p. 4414, 2021.
- [5] S. Taravati, “Spatiotemporal photon blockade for nonreciprocal quantum absorption,” *arXiv preprint arXiv:2409.08137*, 2024.
- [6] S. Taravati and G. V. Eleftheriades, “4D wave transformations enabled by space-time metasurfaces: Foundations and illustrative examples,” *IEEE Antennas Propag. Mag.*, vol. 65, no. 4, pp. 61–74, 2023.
- [7] S. Taravati, “Efficient nonreciprocal frequency conversion with space-time Josephson junction metasurfaces,” in *2024 54th European Microwave Conference (EuMC)*. IEEE, 2024, pp. 600–603.
- [8] J. Sisler, P. Thureja, M. Y. Grajower, R. Sokhoyan, I. Huang, and H. A. Atwater, “Electrically tunable space-time metasurfaces at optical frequencies,” *Nat. Nanotechnol.*, pp. 1–8, 2024.
- [9] S. Taravati, “Designing space-time metamaterials: The central role of dispersion engineering,” *arXiv preprint arXiv:2511.19541*, 2025.
- [10] M. Burla, L. R. Cortés, M. Li, X. Wang, L. Chrostowski, and J. Azaña, “Integrated waveguide Bragg gratings for microwave photonics signal processing,” *Optics express*, vol. 21, no. 21, pp. 25 120–25 147, 2013.
- [11] J. Albert, L.-Y. Shao, and C. Caucheteur, “Tilted fiber Bragg grating sensors,” *Laser & Photonics Reviews*, vol. 7, no. 1, pp. 83–108, 2013.
- [12] S. Song, L. Li, J. Chen, N. Zhong, Y. Liu, Y. He, H. Chang, B. Wan, D. Zhong, and Q. Xie, “Fiber Bragg grating sensor for accurate and sensitive detection of carbon dioxide concentration,” *Sens. Actuator B Chem.*, vol. 404, p. 135264, 2024.
- [13] R. Rohan, K. Venkadeswaran, and P. Ranjan, “Recent advancements of fiber Bragg grating sensors in biomedical application: a review,” *J. Opt.*, vol. 53, no. 1, pp. 282–293, 2024.
- [14] T. A. La, O. Ülgen, R. Shnaiderman, and V. Ntziachristos, “Bragg grating etalon-based optical fiber for ultrasound and optoacoustic detection,” *Nat. Commun.*, vol. 15, no. 1, p. 7521, 2024.
- [15] X. Xue, X. Han, L. Li, L. Min, D. You, and T. Guo, “Real-time monitoring of human breathing using wearable tilted fiber grating curvature sensors,” *J. Light. Technol.*, vol. 41, no. 13, pp. 4531–4539, 2022.
- [16] F. Brückerhoff-Plückelmann, T. Buskasper, J. Römer, L. Krämer, B. Malik, L. McRae, L. Kürpick, S. Palitza, C. Schuck, and W. Pernice, “General design flow for waveguide Bragg gratings,” *Nanophotonics*, vol. 14, no. 3, pp. 297–304, 2025.
- [17] H. J. Eichler, P. Günter, and D. W. Pohl, *Laser-induced dynamic gratings*. Springer, 2013, vol. 50.
- [18] S. Taravati and A. A. Kishk, “Dynamic modulation yields one-way beam splitting,” *Phys. Rev. B*, vol. 99, no. 7, p. 075101, Jan. 2019.
- [19] S. Taravati, “Giant linear nonreciprocity, zero reflection, and zero band gap in equilibrated space-time-varying media,” *Phys. Rev. Appl.*, vol. 9, no. 6, p. 064012, Jun. 2018.
- [20] S. Taravati and A. A. Kishk, “Space-time modulation: Principles and applications,” *IEEE Microw. Mag.*, vol. 21, no. 4, pp. 30–56, 2020.
- [21] S. Taravati and G. V. Eleftheriades, “Generalized space-time periodic diffraction gratings: Theory and applications,” *Phys. Rev. Appl.*, vol. 12, no. 2, p. 024026, 2019.
- [22] S. Taravati and A. A. Kishk, “Advanced wave engineering via obliquely illuminated space-time-modulated slab,” *IEEE Trans. Antennas Propagat.*, vol. 67, no. 1, pp. 270–281, 2019.
- [23] S. Taravati and G. V. Eleftheriades, “Full-duplex nonreciprocal beam steering by time-modulated phase-gradient metasurfaces,” *Phys. Rev. Appl.*, vol. 14, no. 1, p. 014027, 2020.
- [24] S. F. Koufidis, T. T. Koutserimpas, and M. W. McCall, “Temporal analog of Bragg gratings,” *Optics Letters*, vol. 48, no. 17, pp. 4500–4503, 2023.
- [25] S. Taravati and G. V. Eleftheriades, “Microwave space-time-modulated metasurfaces,” *ACS Photonics*, vol. 9, no. 2, pp. 305–318, 2022.
- [26] S. Taravati, A. A. Kishk, and G. V. Eleftheriades, “Finite-difference time-domain simulation of wave transmission through space-time-varying media,” *arXiv preprint arXiv:2409.19923*, 2024.
- [27] S. Taravati, “One-way absorption and isolation in space-time-periodic superconducting metasurfaces,” in *2024 Eighteenth International Congress on Artificial Materials for Novel Wave Phenomena (Metamaterials)*. IEEE, 2024, pp. 1–3.
- [28] S. Taravati and G. V. Eleftheriades, “Lightweight low-noise linear isolator integrating phase-and amplitude-engineered temporal loops,” *Adv. Mater. Technol.*, p. 2100674, 2021.
- [29] A. Alex-Amor, G. Ptitsyn, and N. Engheta, “Kapitza-inspired stabilization of non-foster circuits via time modulations,” *Phys. Rev. Appl.*, vol. 24, no. 2, p. 024022, 2025.
- [30] S. Taravati, “Light transmission through space-time-modulated Josephson junction arrays and application to quantum angular-frequency beam multiplexing,” *IEEE Trans. Antennas Propagat.*, 2025.
- [31] G.-B. Wu, J. Y. Dai, Y. Sun, K. M. Shum, K. F. Chan, Q. Cheng, T. J. Cui, and C. H. Chan, “A space-time holographic metasurface antenna,” *Sci. Adv.*, vol. 11, no. 38, p. eadx7090, 2025.
- [32] S. Taravati, “Self-biased broadband magnet-free linear isolator based on one-way space-time coherency,” *Phys. Rev. B*, vol. 96, no. 23, p. 235150, Dec. 2017.
- [33] S. Taravati and G. V. Eleftheriades, “Space-time medium functions as a perfect antenna-mixer-amplifier transceiver,” *Phys. Rev. Appl.*, vol. 14, no. 5, p. 054017, 2020.
- [34] A. Das and D. H. Werner, “Electrical resonances and power transfer mechanisms for time-varying circuits and systems,” *AIP Advances*, vol. 15, no. 11, 2025.
- [35] S. Taravati and G. V. Eleftheriades, “Pure and linear frequency-conversion temporal metasurface,” *Phys. Rev. Appl.*, vol. 15, no. 6, p. 064011, 2021.
- [36] S. Taravati, “Aperiodic space-time modulation for pure frequency mixing,” *Phys. Rev. B*, vol. 97, no. 11, p. 115131, 2018.
- [37] S. Moreno-Rodríguez, A. Alex-Amor, P. Padilla, J. F. Valenzuela-Valdés, and C. Molero, “Space-time metallic metasurfaces for frequency conversion and beamforming,” *Phys. Rev. Appl.*, vol. 21, no. 6, p. 064018, 2024.
- [38] M. Nadi, A. Cheldavi, and S. H. Sedighi, “Beam steering toward multibeam radiation by time-coding metasurface antennas,” *IEEE Transactions on Antennas and Propagation*, vol. 72, no. 6, pp. 4829–4838, 2024.
- [39] G.-B. Wu, J. Y. Dai, K. M. Shum, K. F. Chan, Q. Cheng, T. J. Cui, and C. H. Chan, “A synthetic moving-envelope metasurface antenna for independent control of arbitrary harmonic orders,” *Nat. Commun.*, vol. 15, no. 1, p. 7202, 2024.

- [40] S. Taravati, "Frequency-multiplexed millimeter-wave fault-tolerant superconducting qubits enabled by an on-chip nonreciprocal control bus," *arXiv preprint arXiv:2512.17588*, 2025.
- [41] A. Cullen, "A travelling-wave parametric amplifier," *Nat.*, vol. 181, no. 332, February 1958.
- [42] P. Tien and H. Suhl, "A traveling-wave ferromagnetic amplifier," *Proc. IEEE*, vol. 46, no. 4, pp. 700–706, 1958.
- [43] P. Tien, "Parametric amplification and frequency mixing in propagating circuits," *J. Appl. Phys.*, vol. 29, no. 9, pp. 1347–1357, 1958.
- [44] J. Li, C. Shen, X. Zhu, Y. Xie, and S. A. Cummer, "Nonreciprocal sound propagation in space-time modulated media," *Phys. Rev. B*, vol. 99, no. 14, p. 144311, 2019.
- [45] M. Sumetsky, "Transformation and amplification of light modulated by a traveling wave with a relatively low frequency," *Phys. Rev. Res.*, vol. 7, no. 4, p. 043066, 2025.
- [46] S. Taravati, "Nonreciprocal entanglement of frequency-distinct qubits," *Adv. Quantum Technol.*, vol. 8, no. 10, p. e2500171, 2025.